energies

MDPI

Article

Combustion Characteristics of Hydrogen/Air Mixtures in a Plasma-Assisted Micro Combustor

Giacomo Cinieri [1], Donato Fontanarosa [2] and Maria Grazia De Giorgi [1,*]

[1] Department of Engineering for Innovation, University of Salento, 73100 Lecce, Italy
[2] Applied Mechanics and Energy Conversion (TME), KU Leuven, 3001 Leuven, Belgium
* Correspondence: mariagrazia.degiorgi@unisalento.it

Abstract: This work performs an analysis of plasma-assisted non-premixed H_2-air flames in Y-shaped micro combustors in the presence of field emission dielectric barrier discharge (FE-DBD) plasma actuators. The combustion, flow, and heat transfer characteristics are numerically investigated, and the effect of sinusoidal plasma discharges on combustion performance is examined at various equivalence ratios (φ). A coupled plasma and chemical kinetic model is implemented, using a zero-dimensional model based on the solution of the Boltzmann equation and the ZDPlasKin toolbox to compute net charges and radical generation rates. The estimated body forces, radical production rates, and power densities in the plasma regions are then coupled with hydrogen combustion in the microchannel. Plasma-assisted combustion reveals improvements in flame length and maximum gas temperature. The results demonstrate that FE-DBDs can enhance mixing and complete the combustion of unreacted fuel, preventing flame extinction. It is shown that even in cases of radical and thermal quenching, these plasma actuators are essential for stabilizing the flame.

Keywords: microscale combustion; plasma assisted combustion; sinusoidal discharge; microburners; flame wall interaction; plasma actuator; dielectric barrier discharge; plasma; ionization degree; chemical kinetics

Citation: Cinieri, G.; Fontanarosa, D.; De Giorgi, M.G. Combustion Characteristics of Hydrogen/Air Mixtures in a Plasma-Assisted Micro Combustor. *Energies* **2023**, *16*, 2272. https://doi.org/10.3390/en16052272

Academic Editor: Michael Liberman

Received: 31 January 2023
Revised: 19 February 2023
Accepted: 23 February 2023
Published: 27 February 2023

1. Introduction

Micro combustion systems offer several advantages over traditional combustion systems, including a high power density, high efficiency, and low emissions. However, the small scale of these systems can also present challenges in terms of flame stability and extinction [1–3]. Conventional batteries are the most widely used energy source in electronic instrumentation today. However, the low energy density, limited-service life, and difficulty in sourcing and disposal of raw materials are problems to overcome [4–6]. The solution may come through micro combustion systems. In recent years, flame dynamics have been rigorously studied and flame-extinguishing mechanisms have been better understood. Hydrocarbon combustion remains a very common source of energy in the 21st century around the world [7]. They are usable in battery-powered systems where microgeneration of energy is required due to extremely high-power density and very short reactivation cycles, such as micro and picosatellites and remotely piloted aircraft systems (RPAS) [8–10]. It's recalled that hydrocarbon combustion energy density is two orders of magnitude higher than batteries [7]. Studies are conducted primarily on alternative, clean fuels to de-carbonize our power sources such as biofuels, natural gas, ammonia, and hydrogen [11–13]. In previous studies, micro combustion is considered if the combustor physical length scale is below 1 mm [14]. Otherwise, it is called mesoscale combustion. At micro scales, the surface-to-volume ratio is high and surface effects have a large impact on flame behavior [15]. There are some major issues to solve. Microscale power generation faces technological challenges. Power is unsteady due to flame instability leading to structural problems. In addition, many micro combustors have incomplete combustion, producing dangerous flammable exhaust gases, causing flame extinction or flame temperature to decrease or even die out

completely [16]. Studies have examined the role of geometry mixture and velocity in micro combustion [15]. Lee et al. studied the effects of interaction between non-premixed flames on the enlargement of blowout velocity with different nozzles [17]. The wall thickness is also important because the thinner it is, the more it reduces heat flow in the axial direction. Greater thicknesses increase conductivity [15,17]. A solution to these problems can be offered by plasma-assisted combustion, in particular, FE-DBD (Field Emission Dielectric Barrier Discharge) actuators [18]. Plasma is a high-energy state of matter, characterized by the dissociation between electrons and atomic nuclei [19]. The presence of free electrons makes substances in the plasma state good conductors of electricity, even when in other states this is not true, as in the case of air. To reach the plasma state, it is necessary to bring gas to a very high temperature, but it is possible to achieve the state transition also through other methods. One of these is to apply an intense electric field to a gas, at much lower temperatures, exploiting the phenomenon of electric field-induced ionization [20]. Two electrodes can be connected to a high voltage alternating current (AC) power supply, nanosecond pulsed (NS), or direct current (DC) power supply system [21–23]. Plasma also makes ignition available at lower flow rates, thanks to radicals and power densities added to the system [24,25]. DBD actuators in the offset configuration have an electrode buried within a dielectric and another electrode exposed to the fluid in an asymmetrical arrangement [26]. This configuration generates a longitudinal force in the direction from the buried to the exposed electrode. The characteristics that determine the performance of the actuators are a function of the electromagnetic variables as well as the thickness and the material of the dielectric, operating pressure, and temperature [27,28]. Among the earliest work in the literature to control fluids by plasma, it was conducted by Roth et al. [29,30] demonstrating its potential applications. Finally, ionization transforms the chemical composition by generating radicals such as atomic oxygen and hydroxyl groups, which are capable of sustaining combustion reactions. It is possible to modify the flow with the use of the FE-DBD thanks to the electrohydrodynamic force (EHD) by transferring the momentum from the ionized particles of the plasma to the neutral particles of the fluid. Thrust vector control combines electromagnetic control and MHD to realize active flow control. The collisions caused by ionization increase the temperature of the fluid. Some applications are intended to improve aerodynamic performances in boundary layers and separation control [31,32].

FE-DBD actuators have been considered for application to the micro-scale since the typical gap of a few microns reduces the breakdown voltage required for plasma-induced decomposition, as shown by both experiments and theory [9,27]. Consequently, they require low power input to produce stronger momentum, heat addition, and chemistry effects. In FE-DBD actuators, the electrode gap is measured in microns. This distance allows the breakdown limit to be exceeded at a potential on the order of 10^2 V instead of kV [33].

Research in recent years intends to find applications for plasma-assisted combustion in ignition systems, such as gas turbine engines, gasoline engines, and hypersonic engines [34,35]. In particular, the studies analyze ignition, combustion acceleration and lean combustion oxyfuel plasma-assisted combustion (PAC) in Computational Fluid Dynamics (CFD) combustion simulations [36]. In low Reynolds number flows, the flame shape can be greatly altered by the forces generated by the actuators. Tang et al. performed an analysis on the combustion of methane propane and hydrogen showing that the hydrogen flame at the same equivalence ratio had a more stable flame [37]. An AC barrier dielectric discharge has been used to flatten a hydrogen flame in crossflow as proved numerically and experimentally. With plasma, the flame temperature is lower and more extensive, due to the additional mixing and generation of radicals in the plasma region. Hydrogen may be one ideal fuel due to its fast diffusion, but its potential danger of flashback restricts its application. The effects of interaction between non-premixed flames on the enlargement of blowout velocity with different nozzles are reported by Lee et al. [38]. Nakamura et al.

performed an analysis of interactions in micro flames and stressed the importance of the premixing degree of fuel and air [39].

Trying to build a model for PAC with sufficient fidelity to predict its efficacy is not an easy task: plasma effects are a multidisciplinary problem and on different time scales [40]. Electron cross-section data are often missing or incomplete. In our work hydrogen combustion understanding in presence of plasma actuation is still far from being fully understood. Among recent efforts to outline an FE-DBD model, Tholeti developed an atmospheric pressure DBD actuator model demonstrating the feasibility of experimentally and microchannel combustion modeling [27]. A planar offset electrode concept was proposed and then enhanced by Shivkumar et al. [28]. Flow control and plasma-assisted combustion were analyzed using the CFD continuum approach in a T shape chamber H_2/O_2 combustion. The actuator body force and power density actuator were computed by performing PIC/MCC simulations. In the literature, a significant amount of research has been conducted on plasma-assisted combustion at the macroscale, while the investigation of its application to microcombustion, specifically with hydrogen, remains highly restricted. Consequently, a comprehensive study on the chemistry effects coupled with the momentum and joule effect was not considered in the literature. In the context of modeling plasma effects in combustion, kinetic modeling of the plasma is often neglected, and only thermal effects are considered. This choice is frequently dictated by computational limitations related to simulation costs. However, this simplification can compromise the accuracy of predictions on the system behavior, especially in the presence of coupled effects between the plasma and the chemical reaction. So, a two-step plasma-assisted combustion (PAC) simulation modeling is provided in this work splitting PAC simulation. In the first step, a sinusoidal discharge was applied and analyzed through a chemistry zero-dimensional modeling based on the solution of the Boltzmann equation [41]. We used FE-DBD actuators with a potential amplitude of 162.5 V and a frequency of 1 GHz. In this work, the toolbox ZDPlasKin has been used, coupled with the Bolsig+ solver. The predicted mixture compositions, as well as the body forces and power by Shivkumar et al. [28] were then used in the 3D-CFD steady-state simulations of a laminar, reactive microflow. These simulations are based on a continuum Navier–Stokes approach. The flame area, temperature, and concentration of reactants and combustion products in the micro combustor have been analyzed. An extended investigation of the impact of the FE-DBD plasma actuation on the performance of the micro-combustor has been conducted.

2. Test Case

2.1. Micro-Combustor Geometry

The model geometry consists of two inlet channels—one for hydrogen and the other for dry air—and a Y-shaped combustion chamber with a 90° angle and a length of 200 mm (Figure 1). This configuration and channel length were previously reported by Xiang et al. [42]. The walls of the combustion chamber are made of quartz with a thickness of 1 mm. The pressure is maintained at 1 atm and the inlet temperature is 300 K. The cross-section of the ducts is rectangular, with an area of 3.14 mm^2 (Figure 1).

2.2. Plasma Actuator Configuration

Figure 2 shows a schematic view of a DBD actuator, with one electrode embedded under a dielectric layer and the other exposed to the gas. The DBD plasma actuator geometry used in the present calculations is based on the configuration reported by [28]. The dielectric and electrode thicknesses are 4 μm and 1 μm, respectively (Table 1). The electrode has a length of 100 μm and a width equal to the width of the conductive layer. The dielectric is made of silicon nitride and has a thickness of 4 μm. The voltage input is sinusoidal, with a peak-to-peak voltage of 325 V and a DC bias of 162.5 V.

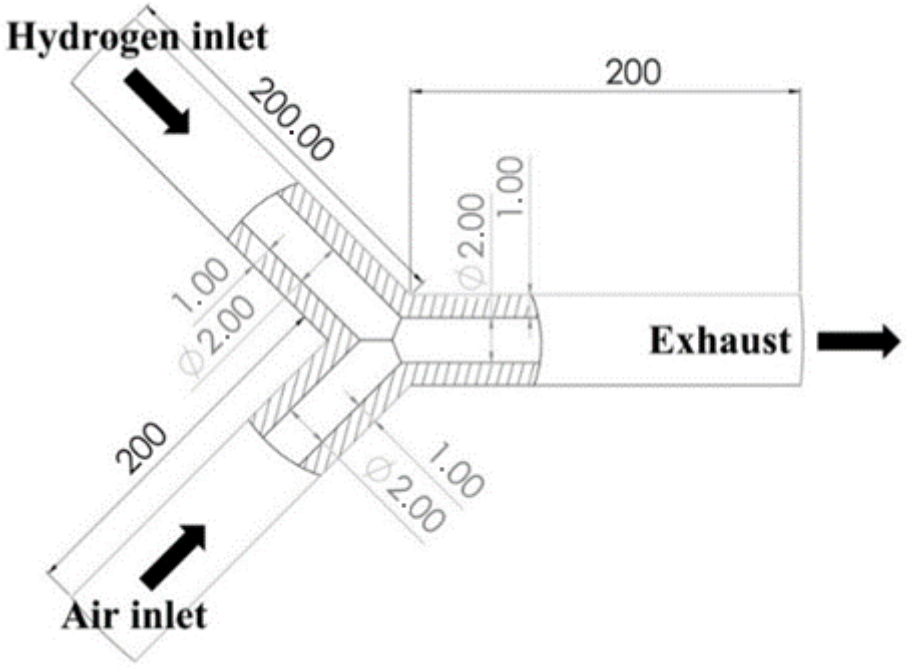

Figure 1. Sketch in mm of the micro combustor.

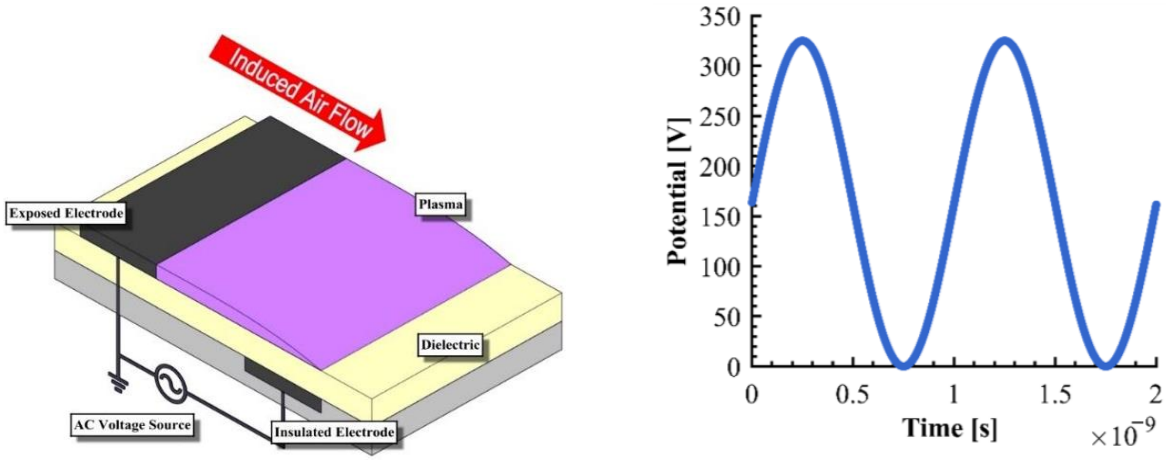

(**a**) (**b**)

Figure 2. FE-DBD offset planar actuator (**a**) general scheme, (**b**) applied potential.

Table 1. Test case geometric and feeding parameters.

Geometric Data	Value
Streamwise Electrodes gap	4×10^{-6} [m]
Electrodes Thickness	1×10^{-6} [m]
Dielectric thickness	1.2×10^{-5} [m]
Electrodes length	1×10^{-4} [m]
Electrodes width	1.57×10^{-3} [m]
Frequency	1 GHz
Amplitude	162.5 V

Mackay et al. [43] studied various designs for actuator positions and body force directions in a Y-shaped combustor geometry. Based on that work, the pump configuration is used to stabilize the flame because it increases the fluid velocity to compensate for potential

viscous losses in the channel, with a longitudinal component of the plasma momentum contribution. Plasma discharges enhance and augment the flames by generating radicals that accelerate the chemical kinetics, body forces that improve fuel/air mixing, and heat generation through Joule heating. An array of nine field emission dielectric barrier discharge (FE-DBD) actuators is positioned in parallel rows on the +y and −y walls in the mixing zone at the entrance of the combustion chamber, with the actuated region extending from x = 0 to x = 5 mm along the x direction (Figure 3). The distance between two adjacent actuators on the same wall is 50 µm. The electrode system, which consists of nine pairs at the entrance of the combustion chamber in the mixing zone, is designed such that the coordinate x = 0 is at the inlet of the combustion chamber, just downstream of the Y-shaped inlet ducts.

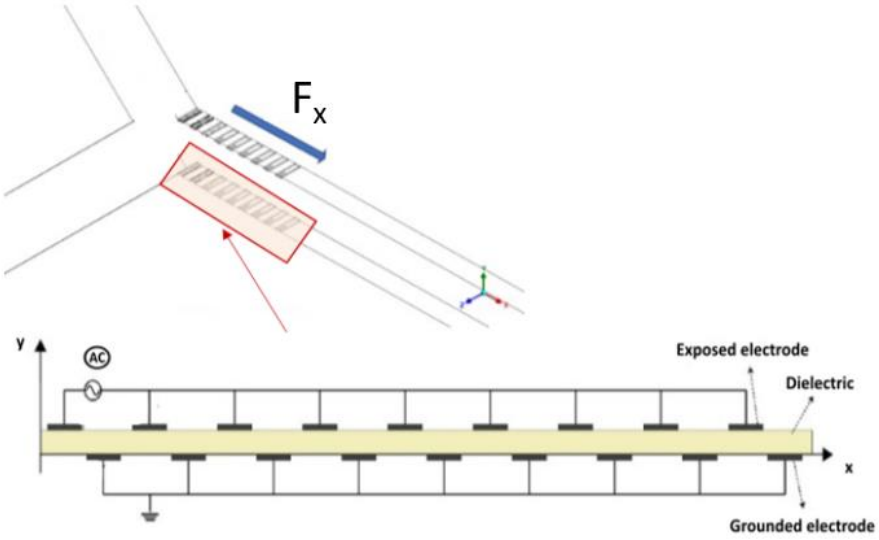

Figure 3. Multi FE-DBD plasma actuators configuration and plasma actuation body force direction.

3. Numerical Model

A coupled plasma and chemical kinetic model has been implemented, with the modeling process consisting of several steps as shown in Figure 4. The characteristic time for plasma dynamics is on the order of 10^{-7} s, while the ignition process is on the order of 10^{-3} s. Therefore, the plasma kinetic modeling has been performed using a zero-dimensional approach based on the solution of the Boltzmann equation. The ZDPlasKin toolbox has been used, along with the Bolsig+ solver, to compute reaction processes and radical generation rates. The estimated body forces, radical production rates, and power densities in the plasma regions are then coupled with hydrogen combustion modeling using a CFD code.

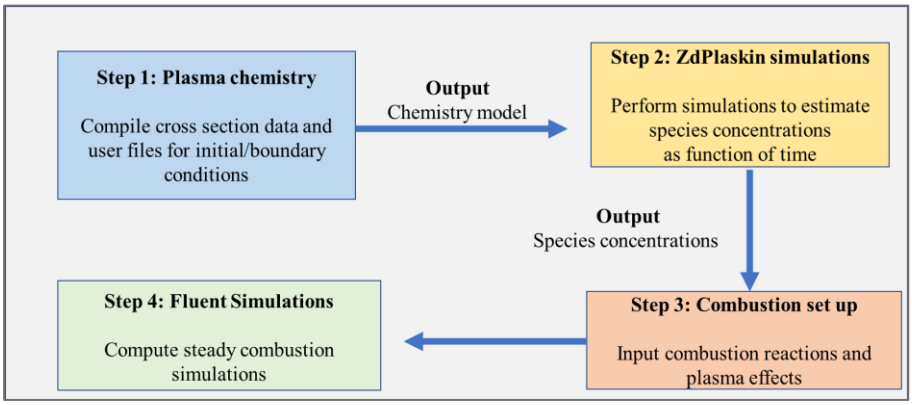

Figure 4. Plasma-assisted combustion methodology.

3.1. CFD Modeling

The equations of continuity, momentum, energy, and conservation of chemical species in the fluid have been discretized using a second-order upwind scheme in the CFD code Fluent 22.0 [44]. The Knudsen number is below 0.01, based on the characteristic length of the microcombustor (microchannel diameter, 0.002 m) and atmospheric conditions, which makes the Navier–Stokes approach appropriate. A segregated solution solver with a sub-relaxation method was used to solve the conservation equations. The SIMPLE pressure-velocity coupling scheme was used, and the pressure spatial discretization was second order. All gradients were calculated using the least squares cell-based scheme. The second-order upwind scheme was applied for momentum, turbulent kinetic energy, turbulent dissipation rate, species, and energy. Results were considered converged when residuals were lower than 10^{-3}, except for continuity. Temperature and combustion product mass fractions were monitored to check simulation convergence and residuals. A three-dimensional steady model was employed, using the Navier–Stokes equations with some assumptions. Viscous forces and gravity were not considered. The basic governing equations of heat and mass transfer are given as follows [45]:

$$\frac{\partial \rho}{\partial t} + \frac{\partial (\rho u_i)}{\partial x_i} = 0 \tag{1}$$

$$\frac{\partial (\rho u_j)}{\partial t} + \frac{\partial \left(\rho u_i u_j - \tau_{ij}\right)}{\partial x_i} = \frac{\partial p}{\partial x_j} + F_{plasma} \tag{2}$$

$$\frac{\partial (\rho h)}{\partial t} + \frac{\partial (\rho u_i h)}{\partial x_i} = \frac{\partial \left(\lambda \partial T_f\right)}{\partial t} - \sum_j \frac{\partial \left(h_j J_j\right)}{\partial x_i} + \sum_j h_j R_j + P_{plasma} \tag{3}$$

$$\frac{\partial (\rho_s c_s T_s)}{\partial t} + \frac{\partial \lambda_s}{\partial x_i}\left(\frac{\partial T_s}{\partial x_i}\right) = 0 \tag{4}$$

$$\frac{\partial (\rho Y_i)}{\partial t} + \frac{\rho u_i Y_i}{\partial x_i} = \frac{\partial J_i}{\partial x_i} - R_i \tag{5}$$

Defining p pressure, ρ gas density, u is the velocity, τ_{ij} is the stress tensor, h is total enthalpy, J_i is the diffusion flux of species i, T is the temperature, R_j is the net rate of production of species j by chemical reaction, Yi is the mass fraction of species i, λ thermal conductivity. F_{plasma} and P_{plasma} are plasma effects added in actuators plasma region.

Shivkumar's work computations [28] proved a fluid time average momentum F_{plasma} of 1.09 $\times$ 10^6 N·m^{-3} and average power density (P_{plasma}) of 1.8 $\times$ 10^9 W/m^{-3} power density in the plasma region [28]. The power input actuator consumes an input power of 2.97 $\times$ 10^2 W m^{-2} [28]. Equation (6) is applied to determine the effect of convection and radiation on the heat losses Q_{loss} [45]:

$$Q_{loss} = h_0 A\ (T_w - T_0) + \varepsilon \sigma A \left(T_w^4 - T_0^4\right) \tag{6}$$

where ε is the wall emissivity, σ is the Stephen-Boltzmann constant, T_w and A are the temperature and surface area of the wall, respectively.

P_1 model defines radiation heat losses. An incompressible ideal gas assumption was adopted. C_p is calculated from mixing law. Mass diffusivity is defined by kinetic theory [46]. The hydrogen/air combustion chemistry is comprised of 11 species and 26 reactions [47], and the interactivity of the turbulence and chemistry was computed by using the Eddy Dissipation Concept (EDC) model since one-step reaction mechanisms cannot reproduce global flame characteristics.

3.2. Plasma Discharge Modeling

ZDPlasKin is a zero-dimensional plasma kinetic solver and two-temperature model tool that uses the Boltzmann Bolsig+ equation solver to solve for the electron density func-

tion and the DVODE 90 solver to provide the chemical differential equation solution [41]. The N_2-H_2-O_2 mixture model includes neutral, metastable, and charged species, with electron cross-section data and impact reactions retrieved from the LXCat website using Phelps and Pancheshnyi databases [48]. The scheme is an extension of the N_2-O_2 mixture scheme, incorporating mixed reactions of N_2-H_2 and H_2-O_2 [49–51]. The initial electron number density is set to 10^{10} m^{-3} for a mixture of air and H_2 (2.0 H_2 + O_2 + 3.76 N_2) at atmospheric conditions. Calculations are performed with a constant time step of 10^{-12} s. A model mechanism has been developed including nitrogen, hydrogen, and oxygen species, with the main species listed in Table 2.

Table 2. Main Particles in the kinetic system.

Species Type	Molecules
Elements	N, H, O
Charged particles	N^+ N_2^+ N_3^+ N_4^+ O^+ O_2^+ O_4^+ O^- O_2^- O_3^- O_4^- NO^+ N_2O^+ NO^- N_2O^- NO_2^- NO_3^- O_2^+ E H^+ H_2^+
Excited species	N_2(A1), N_2(A3), N_2(C3), N_2(V3) N_2(V1), N_2(B3), N_2(V2), N_2(V4) N_2(V7), N_2(V5), N(2D), N_2(V6) N_2(V8) O_2(V1) N(2P) O_2(V2) O(1D) O_2(V3) O_2(B1) O_2(4.5EV) O_2(V4) O_2(A1) O(1S), OH

Kinetics modeling is solved by the following equations [41]:

$$\frac{\mathrm{d}[N_i]}{\mathrm{dt}} - \sum_{j=1}^{j_{max}} Q_{ij}(t) = 0 \tag{7}$$

$$A + bB = \mathrm{cC} + \mathrm{dD} \tag{8}$$

$$k_j[A]^a[B]^b = R_j \tag{9}$$

$$Q_A = -aR,\ Q_B = -bR,\ Q_C = -cR, Q_D = -dR \tag{10}$$

$$\frac{N_{gas}}{\gamma - 1}\frac{\mathrm{d}T_{gas}}{\mathrm{dt}} = \sum_{j=1}^{j_{max}} \delta\varepsilon\ R_j\ P_{elast}\ [N_e] + Q_{src} \tag{11}$$

where N_i is considered the density of the species, Q_{ij} species production rate, R_j is the reaction rate for reaction j, A, B, and C are the species participating in the reactions, a, b, and c are the stoichiometric coefficients.

The plasma is assumed to be uniform during ignition, as confirmed by iCCD imaging that calculates electron-ion recombination reactions, excitation and de-excitation, attachment, and detachment of electrons and neutral species [52]. The gap air potential is calculated at each time step using the output of Orlov's lumped electrical equivalent circuit model, as shown in Figure 5 [53]. The reduced electric field in the model is estimated based on the potential feeding, device geometry, and electric/dielectric materials (Equations (12)–(14)). A capacitor and resistor in parallel are used to describe the fluid, in addition to a capacitor for the dielectric layer [53].

$$C_a = \frac{\varepsilon_0\ \varepsilon_a\ h\ z}{L_p} \tag{12}$$

$$C_d = \frac{\varepsilon_0\ \varepsilon_d\ h_d\ z}{L_d} \tag{13}$$

$$R = \frac{\rho_a\ L_p}{h\ z} \tag{14}$$

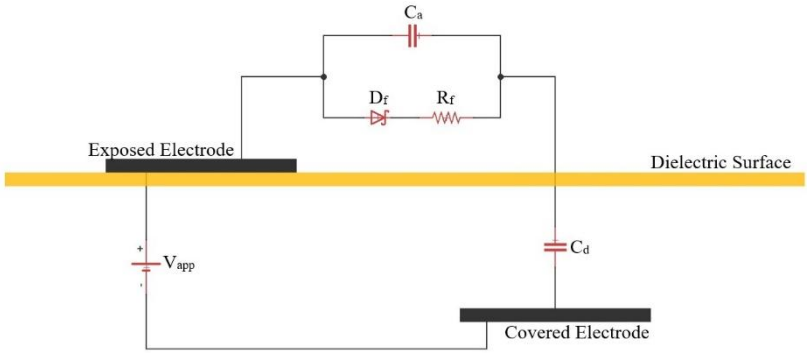

Figure 5. Equivalent plasma actuator lumped electrical circuit.

ε_0 is the vacuum permittivity equal to 8.854 $\times$ 10^{-12} F/m, ε_a is the medium relative permittivity (assumed equal to 1), and ρ_a is the effective resistivity taken equal to 2.3 $\times$ 10^6 Ω·m, h z and L are geometric parameters. An applied sinusoidal potential is equal to:

$$\phi_a(t) = \phi_{amplitude}\ sin\ (2\ \pi\ \omega\ t) + \phi_{bias} \tag{15}$$

Consequently, the discharge potential $\Delta\phi$ is introduced at each time step by applying Kirchoff's law [49]. At the end, it's defined as the reduced electric field, E_N as [49]:

$$E_N = \left| \frac{\Delta\phi}{h\ N_{neutral\ species}} \right| \tag{16}$$

where $N_{neutral\ species}$ is the number density of all neutral species, $\Delta\phi$ is potential difference and h is the plasma height assumed equal to 5 $\times$ 10^{-4} m. At each time step reaction rate and products particles densities have been calculated.

3.3. Computational Domain and Boundary Conditions

Hydrogen and air were injected into two separate channels with constant velocity profiles (Table 3) and a temperature of 300 K. The equivalence ratio, defined as the ratio of hydrogen to air, was set to 0.5 and 0.8.

Table 3. Inlet velocity conditions.

$V_{mixture}$	φ	V_{H_2} [m/s]	V_{air} [m/s]
1	0.5	0.17	0.83
2	0.5	0.34	1.66
6	0.5	1	5
1	0.8	0.24	0.76
2	0.8	0.49	1.51
6	0.8	1.46	4.56

A pressure-outlet boundary condition of 101,325 Pa was set at the outlet, and no-slip conditions were applied to wall boundaries. Combustion simulations were performed at different equivalent fuel/air ratios, with heat transfer to the surroundings accounted for by adopting mixed thermal conditions on the walls of the microcombustor (internal and external emissivity of 0.8 and 0.75, respectively, and a heat transfer coefficient of 20 W/m^2K). The specific heat capacity of quartz glass is 750 J/kg-K and its thermal conductivity is 1.05 W/m-K. A constant free stream temperature of 300 K and wall thickness of 1 mm was used. To simulate the use of a butane torch for ignition in experiments [49], we applied a patch of 2000 K in the last 20 mm of the combustor channel for 5 s. The computational domain has the origin of the coordinate system at the geometric center of the inlet section of the combustion chamber. The x-axis is the longitudinal axis, with a positive direction

towards the outlet in the XY symmetry plane. Since the phenomenon is symmetrical with respect to the *z*-axis, the geometry is halved and a symmetry boundary condition is applied. In the Z direction, three cells were defined due to the symmetric field and low gradient in this direction. The mesh is composed of hexahedral cells, except in the confluence zone where prismatic cells are used (Figure 6). In addition, the mesh is further refined in the plasma regions. The three channels in the experimental design have a diameter of 2 mm, but in the present work, a constant rectangular channel section was used with the same area due to the planar electrode system attached to the wall for plasma-assisted combustion and to maintain the same flow rates [42].

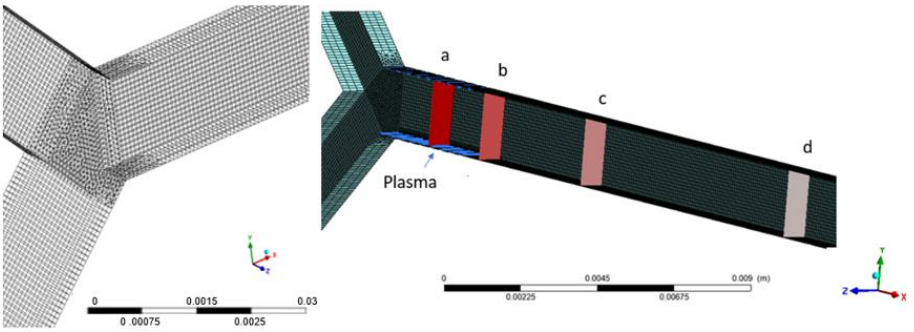

Figure 6. Mesh (**a**) Mixing zone mesh refinement, (**b**) ZY sections whose coordinates are equal to x equal to 2, 5, 10, and 20 mm (x = 0 combustor inlet).

The plasma effects are coupled to the flow in the microchannel through momentum and energy source terms, as described by Tholeti et al. [27]. The concentration of species produced by the plasma discharges, as obtained from ZDPlasKin simulations, is set in the area close to the plasma actuators. The body force and power density values estimated by Shivumkar et al. [28] and listed in Table 4 are used in the plasma zones. The rectangular cross-section is 200 × 50 µm in the XY plane and extends across the width of the combustion chamber wall (0.785 mm, taking into account the symmetry boundary condition) [28].

Table 4. Body force and Power density from Shivumkar et al. [28].

Performance	Value
Body force [N/m^3]	1.06×10^6
Power density [W/m^3]	1.8×10^9

Hydrogen Combustion Validation

For φ lower than 0.5, neither numerical simulations nor experiments show the presence of a flame in the combustion chamber. When the fuel-to-air ratio (φ) is greater than 0.5, a stationary flame forms in the mixing zone. To ensure the accuracy and efficiency of the modeling, a study was conducted to identify the optimal mesh structure by testing three different mesh resolutions of 189 k cells, 237 k cells, and 400 k cells. The simulation of hydrogen/air combustion at inlet velocities of 4.28 m/s for air and 1.28 m/s for hydrogen, which corresponds to an equivalence ratio of 1, was used in this study. The predicted centerline temperature distributions, as shown in Figure 7, demonstrate that the centerline wall temperature profile of the mesh structure with 189 k elements differs slightly from the others in the inlet area of the combustor. However, overall, the three temperature profiles show good agreement. The maximum temperature predicted in the domain was similar for all mesh resolutions, with a maximum 1.2% variation from the coarsest mesh structure, as indicated in Table 5 and Figure 7. Therefore, a mesh structure of 189 k elements was chosen for the present study based on these results.

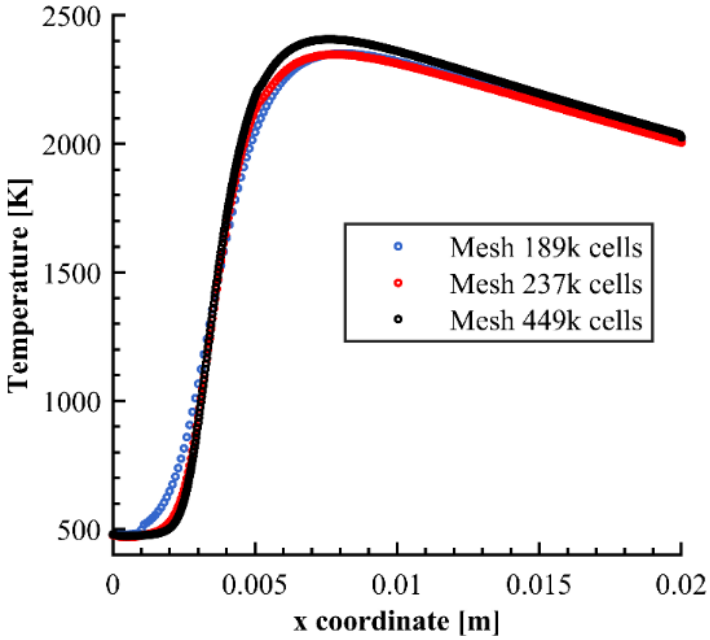

Figure 7. Grid independence symmetry plane chamber midline flame zone. V = 6 m/s, φ = 1.

Table 5. Mesh independence analysis.

Mesh	Cells × 10^3	Max Temperature [K]	Difference %
1	189	2351	0
2	240	2347	0.19%
3	400	2382	1.2%

OH mass fraction and flame emission distribution were found in the inlet intersection for equivalence ratios ranging from 0.6 to 1.4.

In addition, the numerical prediction of the flame length was compared with the experiments conducted by Xiang et al. [42]. To compare the numerical chemical flame length with the experimental visible flame length, a method must be chosen to define the numerical chemical flame length. The chemical flame length is generally wider than the visible flame length, but there are differences between the measured OH fluorescence intensity and the actual OH mole fraction. Moreover, the light intensity field and distances may not always be available, as in this case, but the average position of the stationary luminous flame edges can still be determined. Many of the issues discussed above and in other literature proposals cannot easily be included in a computational flame length methodology, making the quantitative assessment of the measured intensity field difficult [54]. In this work, a good correlation was found between the experimental and predicted flame lengths for reactions that emitted heat greater than 1 W/m^3, temperature greater than 2000 K, and OH mass fraction greater than 0.001. As shown in Figure 8, the flame is always located in the mixing zone as detected experimentally. It is also displaced towards the oxygen inlet, as evidenced by the temperature, heat, and OH mass fraction distribution.

There is a good agreement between the experimental and predicted flame lengths, as shown in Figure 9.

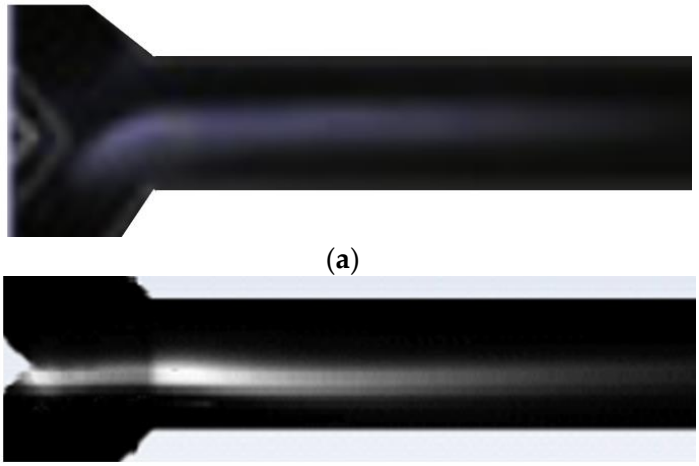

Figure 8. Mixing zone combustor flame. (**a**) On the top experimental picture, (**b**) grayscale of heat emission predicted by CFD simulation. Mixture conditions are V = 6 m/s and φ = 1.

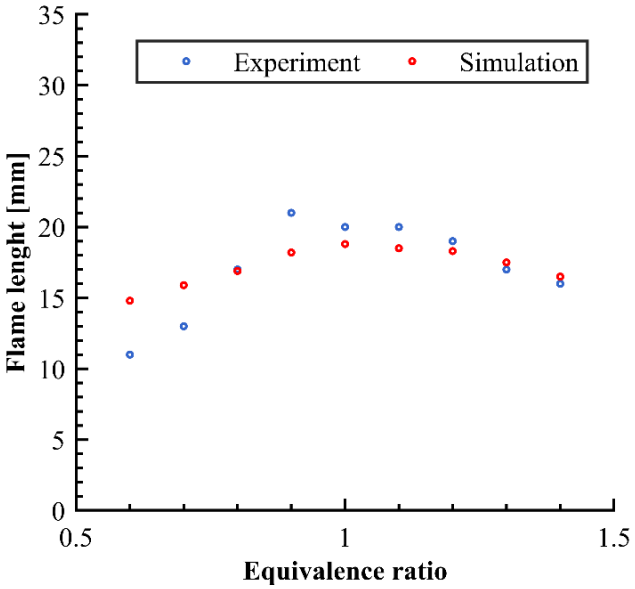

Figure 9. Comparison between experimental visible average flame length [42] and predicted flame length.

4. Results

4.1. Plasma Discharge Kinetic Results

ZDPlasKin tool was used to solve chemical reactions. A stationary solution was reached at a time of 10^{-6} s. Figure 10 shows the estimated reduced electric field E_N, which exhibits a sinusoidal behavior with a maximum of around 400 Td. The same figure also shows the temporal evolution of the concentration of the main species (OH, HO_2, H, H_2O) produced by the plasma discharges. The H atoms formed by H_2 dissociation initiate the fuel oxidation process by producing HO_2. Most of the HO_2 is then converted to OH, and finally, OH reacts with H_2 to produce H_2O, the final product. The particle density values reached at the steady state for the species are converted into mass fractions and used to define the species concentrations in the plasma regions of the actuators for use in the CFD simulations. The final values are shown in Table 6.

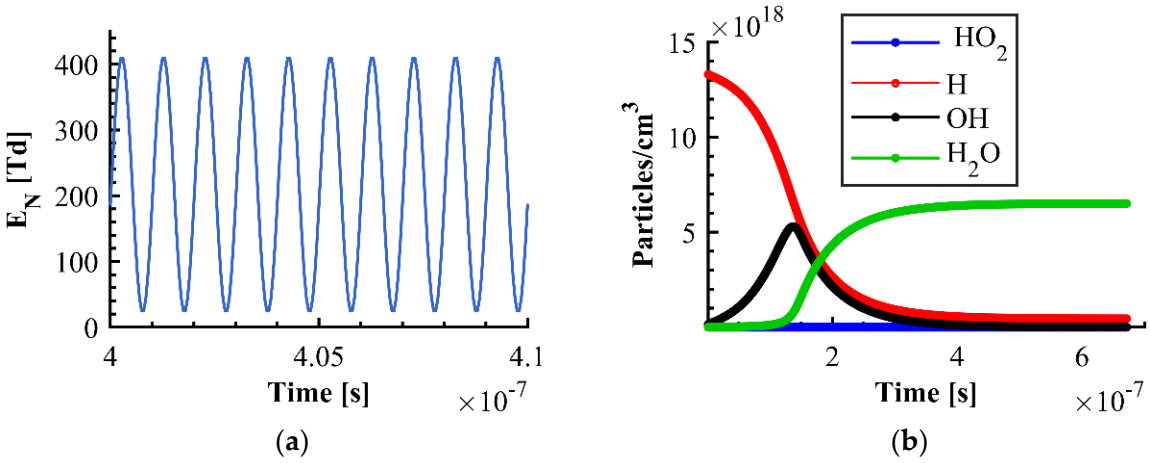

Figure 10. (**a**) Predicted reduced electric field cycles E_N, (**b**) predicted main species particles density over time.

Table 6. ZDPlasKin predicted main species concentration.

Species	Species Density [Particles/cm^3]	Mass Fraction
H	4.38×10^{17}	1.4×10^{-2}
OH	1.44×10^{15}	4.0×10^{-5}
H_2O	6.52×10^{18}	2.1×10^{-1}
HO_2	8.34×10^{13}	2.0×10^{-6}

4.1.1. PAC for φ = 0.5

The flame behavior under the plasma effect has been compared to the case without actuation (clean case, W/O PAC): temperature and species distributions were studied for mean mixture velocities at the inlet of the combustion chamber of 1 m/s, 2 m/s, and 6 m/s, using two different equivalence ratios. For φ equal to 0.5, the W/O PAC steady-state simulations did not produce any combustion, as was also observed in experimental data. In the area of the plasma discharges, both an EHD force and Joule heating acted on the flow, resulting in the acceleration and heating of the air flowing into the plasma region.

Figure 11 illustrates the path lines of combustion with and without the use of PAC at a velocity of 1 m/s. The plasma discharges generate heat and momentum that accelerate the fluid near the plasma actuators, leading to improved mixing in the channel and a speed of 11 m/s in section b. An upward suction effect can be observed upstream of the actuators. The flow encounters the surface of the plasma actuators near the exposed electrode edge and then moves downstream along the dielectric surface, in accordance with [43,55].

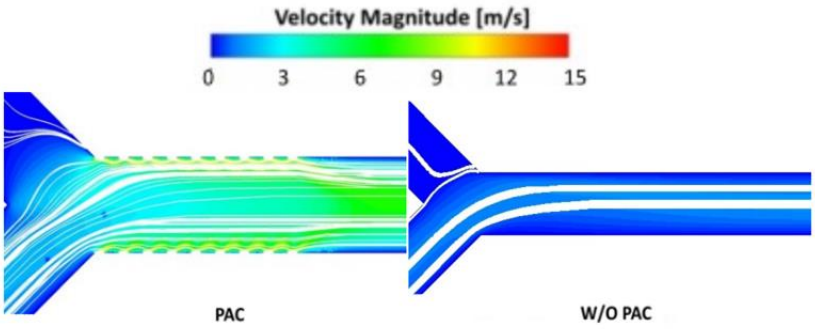

Figure 11. Velocity contour and path lines in the mixing zone for PAC test case in the following conditions: V = 1 m/s and φ = 0.5.

Plasma actuation was able to sustain a stable flame under all tested conditions thanks to the heat and initial chemical radicals. Thus comparing to the results obtained from the investigation realized by Mackay, it is evident in the same way the stabilization of flame in lower fuel concentration mixtures [55].

At an inlet velocity of 1 m/s, the concentration of reactants in the microcombustor is low, leading to a decrease in the heat released by combustion. At this velocity, the combustion reaction zone is closer to the inlet, resulting in a significant heat loss during the flame's downstream transfer. This can be seen in Figure 12, where the peak temperature is low. The flame originates from the electrode zones and moves toward the midline. In section b, the maximum temperature reaches 1777 K, but due to heat loss through the walls, the temperature decreases to 1168 K in section c and 725 K in section d.

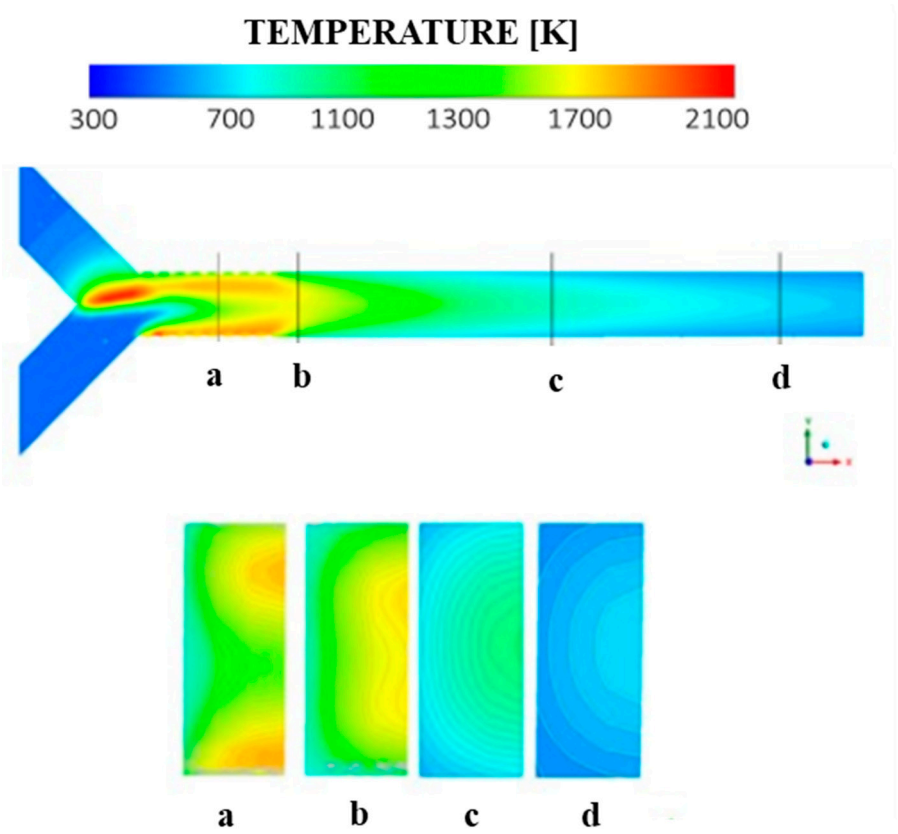

Figure 12. Temperature contours for PAC case at inlet mixture velocity equal to 1 m/s and $\varphi = 0.5$ in symmetry plane and in four YZ sections (a, b, c, d named in Figure 7).

As the inlet velocity of the hydrogen and air mixture increases, the concentration of the reactants gradually increases as well. This results in an increase in the heat released during the combustion reaction, leading to a corresponding increase in the temperature in the reaction zone. Figure 13 illustrates that the maximum temperature value increases with an increase in the mixture inlet velocity. Furthermore, as the inlet velocity increases, the high-temperature region of the combustion reaction expands and moves from the mixing zone toward the outlet of the microcombustor. The contours of the OH mass fraction, shown in Figure 14, give us insight into the flame area and its formation, as the heat released during the reaction and the highest temperature is closely correlated with the OH mass fraction. In the case of plasma-assisted combustion, the OH mass fraction can be found in both the flame area and the area of plasma discharges near the electrodes. The increase in inlet velocity also affects the formation of OH* due to an improvement in combustion efficiency.

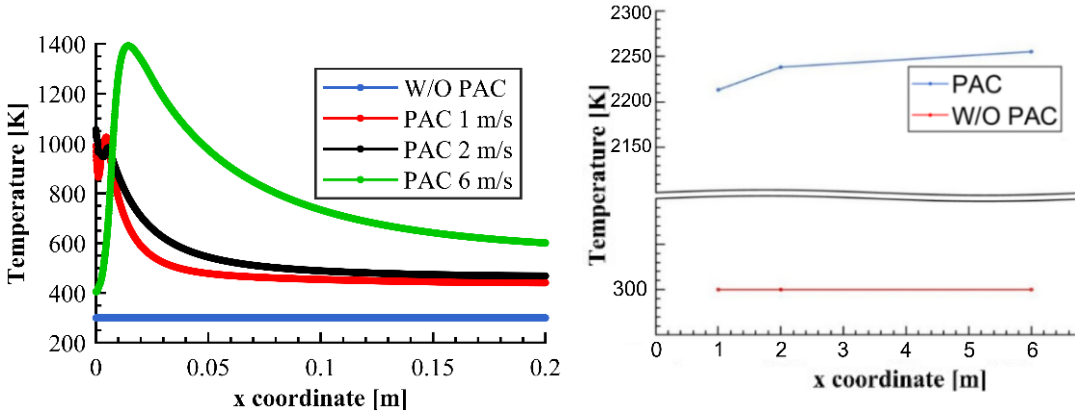

Figure 13. Temperature for the cases at φ = 0.5 and different inlet mixture velocity without (W/O PAC) and with PAC (PAC) (**a**) Chamber midline temperature profiles, (**b**) Max fluid temperature.

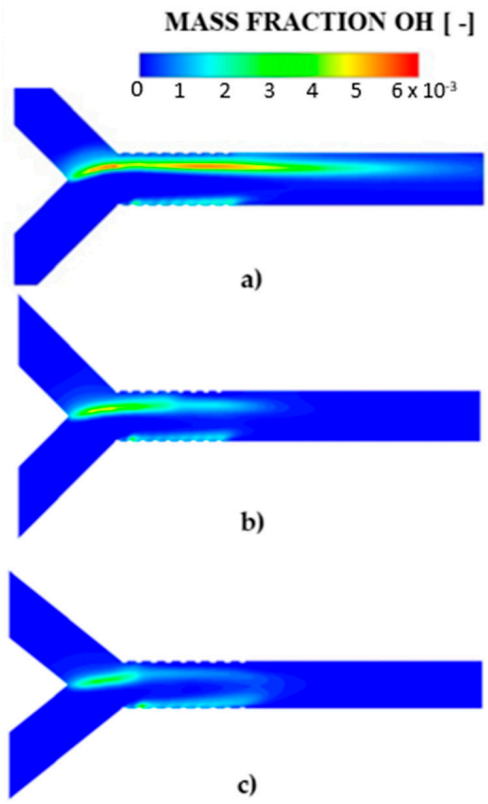

Figure 14. Contours of OH mass fraction for PAC at φ = 0.5 (**a**) 6 m/s, (**b**) 2 m/s, (**c**) 1 m/s.

4.1.2. Plasma-Assisted Combustion for φ = 0.8

In the case of an equivalence ratio of 0.8, steady-state flames were compared with and without plasma assistance. Plasma assistance was found to improve flame ignition and efficiency in both lean and rich mixtures. A comparison of temperature fields at low speeds was conducted in the symmetry and ZY sections. In Figure 15, it can be seen that in both cases, the flame area expands and moves toward the outlet. Additionally, the flame becomes divided between the mixing zone and the plasma area on the air inlet side and moves from the plasma zone toward the center. At a velocity of 2 m/s, the temperature field exhibits a forked flame distribution (as shown in Figure 15a), but the plasma region has an area that is twice as large as the other case at a velocity of 1 m/s.

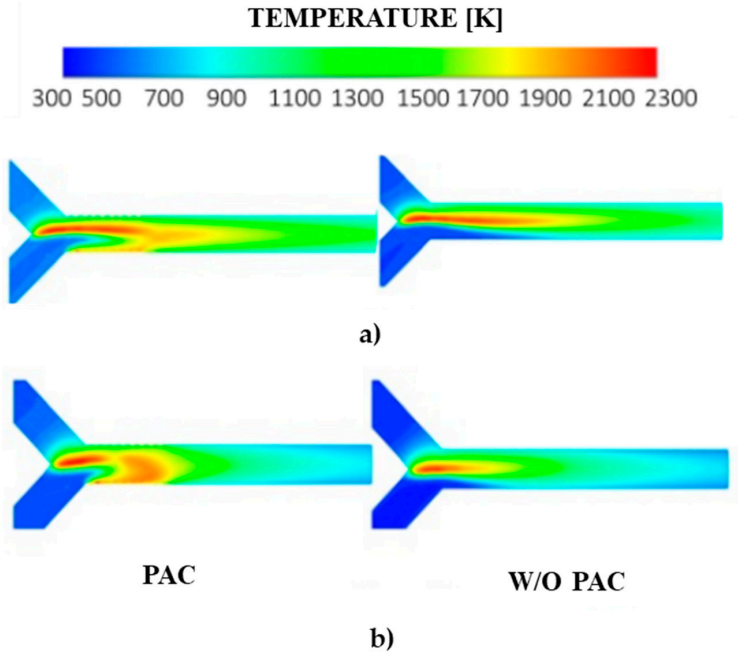

Figure 15. Flame zone temperature contours (**a**) v = 2 m/s, (**b**) v = 1 m/s with plasma actuators (PAC) on the left, and without plasma (W/O PAC) on the right.

In Figure 16, the YZ sections provide a different perspective for comparing flames with and without plasma assistance. The plasma-assisted combustion test case has the highest temperatures in all sections. In the case without plasma, the flame has a symmetrical temperature distribution, while in the plasma-assisted combustion case, the effect of the electrodes is evident in section a, converging in section b. At a velocity of 2 m/s, the maximum temperature in the plasma-assisted combustion test case in section d is 1175 K, while in the other cases, it reaches 1011 K, demonstrating improved performance and a longer flame area. At a velocity of 1 m/s, the plasma temperature reaches 660 K in section d, just 30 K higher than the baseline test case without plasma assistance.

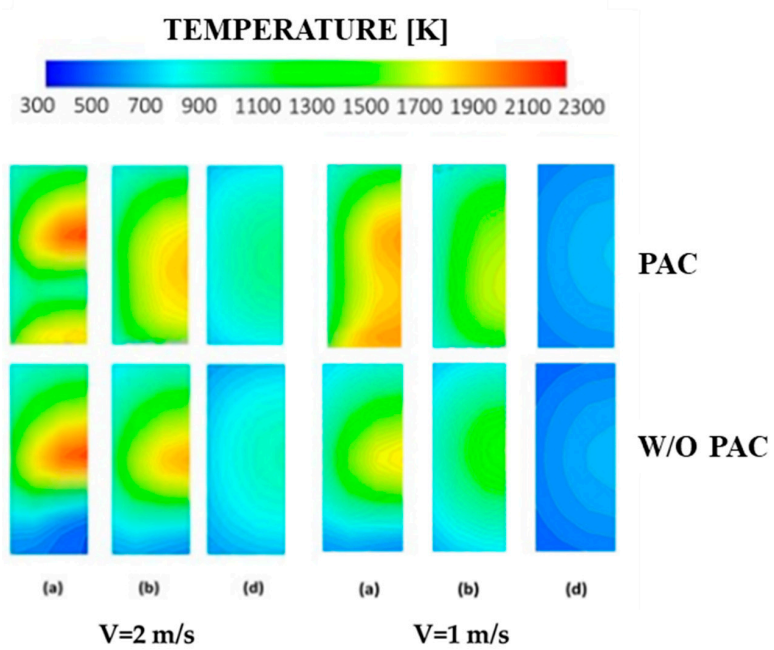

Figure 16. Flame zone temperature. First row: PAC, Second Row: W/O PAC. First column V = 2 m/s, second column V = 1 m/s. The labels a, b and d are named in Figure 7.

At V= 6 m/s, plasma assistance in combustion does not significantly affect the main flame area and OH mass fraction distribution compared to the previous test cases, but higher temperatures are still achieved in all sections and throughout the domain (Figure 17). A bifurcated flame is still obtained in this case. In section d, the temperature in the plasma-assisted combustion (PAC) case is equal to 1945 K, while in the baseline case it is 1887 K, indicating improved overall performance and an extended flame area. As shown in Figure 18, plasma-assisted combustion consistently results in higher temperatures compared to cases without plasma assistance across all test cases.

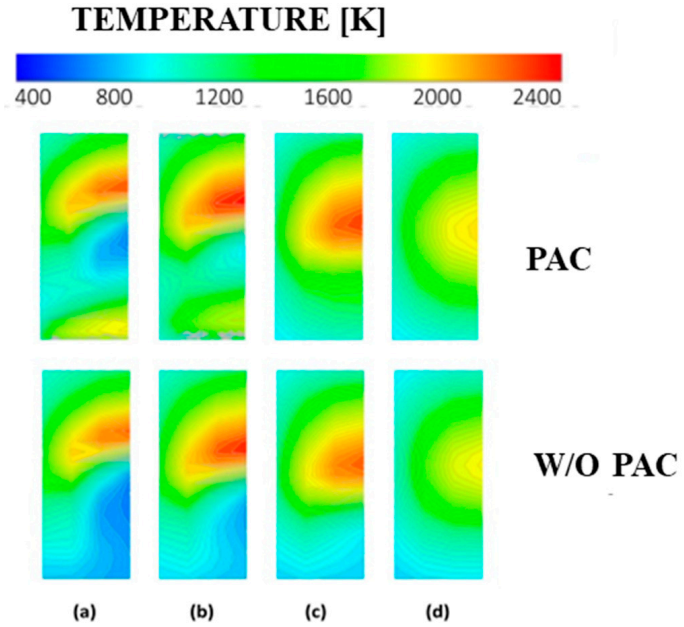

Figure 17. Temperature contours 6 m/s. First row: PAC, Second Row: W/O PAC. The labels a, b, c, and d are named in Figure 7.

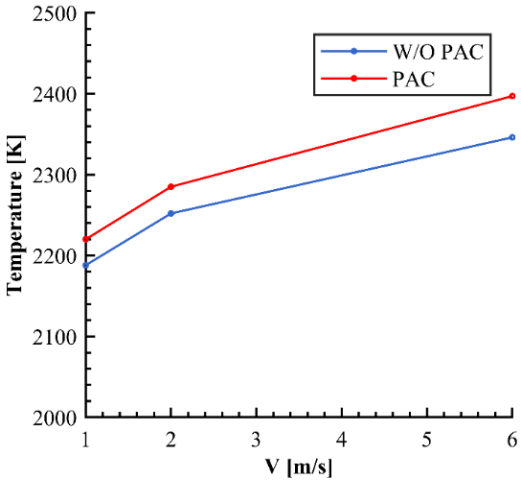

Figure 18. Max fluid temperature for φ = 0.8 and different inlet velocity, without (W/O PAC) and with PAC (PAC).

4.1.3. Efficiency

The efficiency of the system is determined by the ratio of the enthalpy increase between the inlet and outlet to the total input thermal power, which is equal to the output chemical

power from the complete combustion of hydrogen and the input power of the actuators (Equation (17)) [56].

$$\eta = \frac{\dot{m}_{exit}\, c_p\, T_{exit} - \dot{m}_{inlet}\, c_p\, T_{inlet}}{\dot{m}_{hydrogen}\, LHV_{hydrogen} + P_{actuators}} \quad (17)$$

where $LHV_{hydrogen}$ is the low heating value of hydrogen. The results showed that the efficiency of the system is significantly less impacted by the power of the plasma discharge than by the power of the combustion. Each actuator consumes 2.97×10^2 W m^{-2}, resulting in a total power of approximately 0.25 W for the entire chamber, approximately one order of magnitude less than the fuel power output, in accordance with [28,43]. The lowest heating value of hydrogen is around 1.19×10^8 J/kg. In the test case with the lowest hydrogen flow rate (V = 1 m/s and φ = 0.5), the fuel power is about 2.6 W. Table 7 illustrates the system efficiency. Plasma-assisted combustion enhances lean mixtures, increasing velocities, maximum temperatures, and the size of the stable flame area. At low inlet velocities, the concentration of reactants in the microcombustor is low, resulting in a low heat release from combustion. This is exacerbated by the proximity of the combustion zone to the inlet, leading to a significant heat loss as the flame is transported downstream. As the inlet velocity increases, the concentration of reactants increases, leading to an increase in the heat released by the combustion of hydrogen/air and a corresponding rise in temperature in the reaction zone. Over 99% of the hydrogen that enters the burner is effectively consumed, as found also in [28,55]. The exhaust gases are primarily composed of oxygen, nitrogen, and water vapor, as also reported in [28]. Our findings were compared to those of previous literature studies, and it was observed that the microcombustion efficiency of a T-shaped H_2-air stoichiometric microcombustion, as provided by plasma actuators, was 21.9%, which is similar to our best configuration [56]. Our device's efficiency was found to be superior to Mackay's Y-shaped microcombustor PAC analysis, with our efficiency being up to 10 times higher in certain cases [43]. The primary reason for this improvement can be attributed to the differences in geometry, with our combustion chamber being significantly longer. This allows for higher flow rates, resulting in almost complete combustion of the hydrogen and fewer quenching phenomena. Moreover, the significant contribution of radical analysis in plasma discharge performed significantly improved the combustion and overcame pressure gradients and wall heat losses, as discussed in previous chapters.

Table 7. Predicted efficiency.

φ	*V* [m/s]	η_{PAC}	$\eta_{W/O\ PAC}$
0.5	1	0.10	0
0.5	2	0.06	0
0.5	6	0.22	0
0.8	1	0.09	0.02
0.8	2	0.13	0.11
0.8	6	0.16	0.12

5. Conclusions

This paper investigates the development of a new multiscale modeling framework for simulating dielectric barrier discharge (DBD) plasma actuators in a microcombustor for enhancing combustion. The framework combines a microscopic plasma kinetic model with a macroscopic CFD plasma-fluid model, allowing for a detailed description of the plasma without the need for computationally expensive calculations. The proposed microscopic plasma kinetic model is used to estimate the species mass fractions in the plasma regions, which are then used in the plasma-fluid model. The main conclusions are:

- The impact of plasma was observed in multiple configurations with a significant impact on performance improvement, particularly in the leanest mixtures where plasma is necessary for achieving a stationary flame.

- When comparing the lean condition to the clean case, the combustion efficiency is 0.22 at the maximum mass flow rate analyzed. For equivalence ratio equal to 0.8, the efficiency improvement is about 50% compared to the clean case.
- Further experimental studies need to be developed to analyze ignition and flame time development.

Author Contributions: Conceptualization, M.G.D.G. and D.F.; methodology, M.G.D.G. and D.F.; software, G.C. and D.F.; validation, G.C.; formal analysis, D.F.; investigation, G.C.; resources, M.G.D.G.; data curation, G.C.; writing—original draft preparation, G.C.; writing—review and editing, M.G.D.G. and D.F.; visualization, G.C.; supervision, M.G.D.G.; project administration, M.G.D.G.; funding acquisition, M.G.D.G. All authors have read and agreed to the published version of the manuscript.

Funding: This research received no external funding.

Data Availability Statement: The data presented in this study are available on request from the corresponding author.

Conflicts of Interest: The authors declare no conflict of interest.

References

1. Hiranandani, K.; Aravind, B.; Kishore, V.R.; Kumar, S. Development of a numerical model for performance prediction of an integrated microcombustor-thermoelectric power generator. *Energy* **2019**, *192*, 116624. [CrossRef]
2. Wang, S.; Fan, A. Combustion regimes of syngas flame in a micro flow reactor with controlled temperature profile: A numerical study. *Combust. Flame* **2021**, *230*, 111457. [CrossRef]
3. Chouraqui, H.; Dayma, G.; Ribert, G.; Halter, F.; Chauveau, C.; Dagaut, P. Experimental and numerical studies of the diluent influence (N2, Ar, He, Xe) on stable premixed methane flames in micro-combustion. *Proc. Combust. Inst.* **2021**, *38*, 6753–6761. [CrossRef]
4. Jiaqiang, E.; Jiangjun, D.; Jingwei, C.; Gaoliang, L.; Feng, Z.; Bo, L. Process in micro-combustion and energy conversion of micro power system: A review. *Energy Convers. Manag.* **2021**, *246*, 114664.
5. Gao, H.; Li, G.; Zhu, W.; Zheng, D.; Ye, Y.; Guo, W. Experimental study of a mesoscale combustor-powered thermoelectric gen-erator. *Energy Rep.* **2020**, *6*, 507–517. [CrossRef]
6. Van Noorden, R. A better battery. *Nature* **2014**, *507*, 26. [CrossRef] [PubMed]
7. Fernandez-Pello, A.C. Micropower generation using combustion: Issues and approaches. *Proc. Combust. Inst.* **2002**, *29*, 883–899. [CrossRef]
8. De Giorgi, M.G.; Traficante, S.; Ficarella, A. Performance Improvement of Turbomachinery Using Plasma Actuators. In Proceedings of the ASME 2011 Turbo Expo: Turbine Technical Conference and Exposition, Vancouver, BC, Canada, 6–10 June 2011; PARTS A, B, and C. Volume 7, pp. 369–380. [CrossRef]
9. De Giorgi, M.G.; Traficante, S.; De Luca, C.; Bello, D.; Ficarella, A. Active Flow Control Techniques on a Stator Compressor Cascade: A Comparison Between Synthetic Jet and Plasma Actuators. In Proceedings of the ASME Turbo Expo 2012: Turbine Technical Conference and Exposition, Copenhagen, Denmark, 11–15 June 2012.
10. Soni, J.; Zito, J.; Roy, S. Design of a microNewton Thrust Stand for Low Pressure Characterization of DBD Actuators. In Proceedings of the 51st AIAA Aerospace Sciences Meeting including the New Horizons Forum and Aerospace Exposition 2013, Grapeville, TX, USA, 7–10 January 2013; pp. 1–13.
11. Faingold, G.; Lefkowitz, J. A numerical investigation of NH_3/O_2/HE ignition limits in a non-thermal plasma. *Proc. Combust. Inst.* **2021**, *38*, 6661–6669. [CrossRef]
12. Aravind, B.; Hiranandani, K.; Kumar, S. Development of an ultra-high capacity hydrocarbon fuel based micro thermoelectric power generator. *Energy* **2020**, *206*, 118099. [CrossRef]
13. Zuo, W.; Li, Q.; He, Z.; Li, Y. Numerical investigations on thermal performance enhancement of hydrogen-fueled micro planar combustors with injectors for micro-thermophotovoltaic applications. *Energy* **2020**, *194*, 116904. [CrossRef]
14. Maruta, K. Micro and mesoscale combustion. *Proc. Combust. Inst.* **2011**, *33*, 125–150. [CrossRef]
15. Niket, S.K.; Dionisios, G.V. A review on microcombustion: Fundamentals, devices and applications. *Prog. Energy Combust. Sci.* **2012**, *38*, 321.
16. Bucci, M.A.; Robinet, J.-C.; Chibbaro, S. Combustion and Flame. Global stability analysis of 3D micro-combustion model. *Combust. Flame* **2016**, *167*, 132–148. [CrossRef]
17. Lee, I.C. *Small Scale Burner Review*; Technical Report; Army Research Lab: Adelphi, MD, USA, 2009; p. 28.
18. Corke, T.C.; Enloe, C.L.; Wilkinson, S.P. Dielectric Barrier Discharge Plasma Actuators for Flow Control. *Annu. Rev. Fluid Mech.* **2010**, *42*, 505–529. [CrossRef]
19. Abdollahzadeh, M. Analysis and Development of Numerical Methodologies for Simulation of Flow Control with Dielectric Barrier Discharge Actuators. Ph.D. Thesis, Universidade da Beira Interior, Covilhã, Portugal, 2014.

20. Laroussi, M. Low Temperature Plasma-Based Sterilization: Overview and State-of-the-Art. *Plasma Process. Polym.* **2005**, *2*, 391–400. [CrossRef]
21. Zheng, B.R.; Xue, M.; Ke, X.Z.; Ge, C.; Wang, Y.; Liu, F.; Luo, J. Unsteady vortex structure induced by a trielectrode sliding discharge plasma actuator. *AIAA J.* **2019**, *57*, 1–5. [CrossRef]
22. Corke, T.C.; Thomas, F.O. Active and Passive Turbulent Boundary-Layer Drag Reduction. *AIAA J.* **2018**, *56*, 3835–3847. [CrossRef]
23. Zhang, H.; Wu, Y.; Li, Y.; Yu, X.; Liu, B. Control of compressor tip leakage flow using plasma actuation. *Aerosp. Sci. Technol.* **2019**, *86*, 244–255. [CrossRef]
24. Zhong, H.; Mao, X.; Rousso, A.C.; Patrick, C.L.; Yan, C.; Xu, W.; Chen, Q.; Wysocki, G.; Ju, Y. Kinetic study of plasma-assisted n-dodecane/O_2/N_2 pyrolysis and oxidation in a nanosecond-pulsed discharge. *Proc. Combust. Inst.* **2021**, *38*, 6521–6531. [CrossRef]
25. Starikovskaia, S.; Lacoste, D.A.; Colonna, G. Non-equilibrium plasma for ignition and combustion enhancement. *Eur. Phys. J. D* **2021**, *75*, 231. [CrossRef]
26. Rodrigues, F.; Pascoa, J.; Trancossi, M. Heat generation mechanisms of DBD plasma actuators. *Exp. Therm. Fluid Sci.* **2018**, *90*, 55–65. [CrossRef]
27. Tholeti, S.S.; Shivkumar, G.; A Alexeenko, A. Field emission microplasma actuation for microchannel flows. *J. Phys. D Appl. Phys.* **2016**, *49*, 215203. [CrossRef]
28. Shivkumar, G.; Tholeti, S.S.; Alexeenko, A.A. Microchannel flow enhancement by microplasma actuation. In Proceedings of the ASME 2015 13th International Conference on Nanochannels, Microchannels, and Minichannels collocated with the ASME 2015 International Technical Conference and Exhibition on Packaging and Integration of Electronic and Photonic Microsystems, San Francisco, CA, USA, 6–9 July 2015; p. V001T04A006.
29. Roth, J.; Sherman, D.; Wilkinson, S. Boundary layer flow control with a one atmosphere uniform glow discharge surface plasma. In Proceedings of the 36th AIAA Aerospace Sciences Meeting and Exhibit, Reno, NV, USA, 12–15 January 1998. [CrossRef]
30. Greenblatt, D.; Schneider, T.; Schüle, C.Y. Mechanism of flow separation control using plasma actuation. *Phys. Fluids* **2012**, *24*, 077102. [CrossRef]
31. Zhang, X.; Li, H.; Huang, Y.; Tang, K.; Wang, W. Leading-edge flow separation control over an airfoil using a symmetrical dielectric barrier discharge plasma actuator. *Chin. J. Aeronaut.* **2019**, *32*, 1190–1203. [CrossRef]
32. Zhang, P.F.; Liu, A.; Wang, J. Flow structures in flat plate boundary layer induced by pulsed plasma actuator. *Sci. China Technol. Sci.* **2010**, *53*, 2772–2782. [CrossRef]
33. Svarnas, P.; Giannakopoulos, E.; Kalavrouziotis, I.; Krontiras, C.; Georga, S.; Pasolari, R.; Papadopoulos, P.; Apostolou, I.; Chrysochoou, D. Sanitary effect of FE-DBD cold plasma in ambient air on sewage biosolids. *Sci. Total Environ.* **2019**, *705*, 135940. [CrossRef]
34. Takita, K. Ignition and combustion enhancement by thermal plasma. *J. Combust. Soc. Jpn.* **2009**, *51*, 273–280.
35. Starikovskii, A.Y. Plasma supported combustion. *Proc. Combust. Inst.* **2005**, *30*, 2405–2417. [CrossRef]
36. Sasaki, K.; Yoshihiko, U.; Noriyasu, O.; Yugo, O. Merging plasma science into combustion science—plasma-assisted combustion. *J. Combust. Soc. Jpn.* **2009**, *51*, 259–267.
37. Tang, A.; Xu, Y.; Shan, C.; Pan, J.; Liu, Y. A Comparative Study on Combustion Characteristics of Methane, Propane and Hydrogen Fuels in Micro-Combustor. *Int. J. Hydrogen Energy* **2015**, *40*, 16587–16596. [CrossRef]
38. Lee, B.-J.; Kim, J.-S.; Lee, S. Enhancement of blowout limit by the interaction of multiple nonpremixed jet flames. *Combust. Sci. Technol.* **2004**, *176*, 481–497. [CrossRef]
39. Nakamura, Y.; Kubota, A.; Yamashita, H.; Saito, K. Numerical Study on Structure of Microflame with Detailed Chemistry Model (Strategy to Miniaturization of Microflames). *Trans. Jpn. Soc. Mech. Eng. Ser. B* **2008**, *74*, 699–706. [CrossRef]
40. Thomas, F.O.; Corke, T.C.; Iqbal, M.; Kozlov, A.; Schatzman, D. Optimization of Dielectric Barrier Discharge Plasma Actuators for Active Aerodynamic Flow Control. *AIAA J.* **2009**, *47*, 2169–2178. [CrossRef]
41. Pancheshnyi, S.; Eismann, B.; Hagelaar, G.J.M.; Pitchford, L.C. *Computer Code ZDPlasKin*; University of Toulouse: Toulouse, France, 2008. Available online: http://www.zdplaskin.laplace.univ-tlse.fr (accessed on 1 January 2023).
42. Ying, X.; Shixuan, W.; Zili, Y.; Aiwu, F. Effects of channel length on propagation behaviors of non-premixed H_2-air flames in Y-shaped micro combustors. *Int. J. Hydrogen Energy* **2020**, *45*, 20449–20457.
43. Mackay, K.; Kyle, K.; Johnson, H.T.; Freund, J.B. Field-emission plasma enhancement of H_2–O_2 micro-combustion. *Plasma Sources Sci. Technol.* **2020**, *29*, 045014. [CrossRef]
44. ANSYS FLUENT 12.0 User's Guide. Available online: www.enea.it (accessed on 1 October 2022).
45. Xiao, Y.Y.; Wenming, D.; Shikui, T. Heping, Flame stability analysis of premixed hydrogen/air mixtures in a swirl mi-cro-combustor. *Energy* **2020**, *209*, 118495.
46. Gao, J.; Hossain, A.; Matsuoka, T.; Nakamura, Y. A numerical study on heat-recirculation assisted combustion for small scale jet diffusion flames at near-extinction condition. *Combust. Flame* **2017**, *178*, 182–194. [CrossRef]
47. Yang, X.X.; Shen, J.; Santner, H.; Zhao, Y.J. Princeton HP-Mech. Available online: http://engine.princeton.edu/mechanism/HP-Mech.html (accessed on 10 November 2022).
48. DeFilippo, A.C.; Chen, J.-Y. Modeling plasma-assisted methane–air ignition using pre-calculated electron impact reaction rates. *Combust. Flame* **2016**, *172*, 38–48. [CrossRef]

49. Capitelli, M.; Ferreira, C.M.; Gordiets, B.F.; Osipov, A.I. *Plasma Kinetics in Atmospheric Gases*; Springer: Berlin/Heidelberg, Germany, 2000.
50. Available online: www.lxcat.net (accessed on 10 November 2022).
51. Minesi, N.; Mariotto, P.; Stancu, G.D.; Laux, C.O. Role of the excited electronic states in the ionization of ambient air by a na-nosecond discharge. In Proceedings of the AIAA Scitech Forum 2020, Orlando, FL, USA, 6–10 January 2020.
52. Neretti, G.; Taglioli, M.; Borghi, C.A. Experimental determination and numerical evaluation under simplifying assumptions of the ozone concentration in an atmospheric-pressure air DBD plasma. *Eur. Phys. J. D* **2018**, *72*, 113. [CrossRef]
53. Underwood, T.; Roy, S.; Glaz, B. Development of a Lumped Element Circuit Model for Approximation of Nanosecond Pulsed Dielectric Barrier Discharges. In Proceedings of the 51st AIAA Aerospace Sciences Meeting including the New Horizons Forum and Aerospace Exposition 2013, Grapeville, TX, USA, 7–10 January 2013.
54. Li, J.; Huang, H.; Bai, Y.; Li, S.; Kobayashi, N. Combustion and heat release characteristics of hydrogen/air diffusion flame on a micro-jet array burner. *Int. J. Hydrogen Energy* **2018**, *43*, 13563–13574. [CrossRef]
55. Mackay, K.K.; Freund, J.B.; Johnson, H.T. Enhancement of hydrogen microcombustion via field-emission dielectric barrier discharge. *Plasma Sources Sci. Technol.* **2018**, *27*, 085007. [CrossRef]
56. Shivkumar, G. Coupled Plasma Fluid and Thermal Modeling of Low Pressure and Microscale Gas Discharges. Master's Thesis, Faculty of Purdue University, Gayathri Shivkumar Purdue University, West Lafayette, IN, USA, 2019.